Multimodal Magnetic Soft Robots Enabled by Bistable Kirigami Patterns

Ruichen Wang, Jinqiang Wang, Zixiao Zhu, and Dong Wang

***Abstract*—Creatures in nature have evolved to possess various modes of locomotion as a survival strategy. Drawing inspiration from nature, researchers have developed soft robots capable of achieving multiple modes of motion through multiple actuation controlling and structural reconfiguration. However, the complex control sequences and slow and tethered actuation limit their development. In this study, we introduce untethered soft robots capable of programmable multimodal motion by integrating bistable kirigami structures and hard magnetic actuations. By manipulating the external magnetic field, the soft robots not only undergo rapid transitions between different stable states but also exhibit distinct motions at each state, owing to variations in their geometric configurations and magnetization orientations. To understand the bistable transition behaviors, we develop a theoretical model based on the energy method, which is subsequently validated through finite-element analysis and experiments. Experimental results demonstrate the versatility of the bistable soft robots, including following "L"-shaped trajectories, displaying amphibious behaviors, and serving as recycle stents. The proposed bistable kirigami design and hard-magnetic driven methods open up possibilities for developing next-generation autonomous soft robots.**

***Index Terms*—Bistable kirigami pattern, hard-magnetic actuation, multimodal motions, soft robots.**

I. Introduction

CREATURES in nature have evolved to possess various modes of locomotion as a survival strategy. Consider caterpillars, which can rapidly coil up and roll away from threats in addition to their standard crawling [1], or eagles, which can soar into the sky on their wings and move lightly over land on their feet [2]. The capacity for executing intricate yet controlled multimodal locomotion is a crucial characteristic exhibited by animals. Inspired by nature, researchers have endeavored to create soft robots that emulate the multimodal motions observed in animal behaviors [3], [4], [5], [6], [7], [8]. This emulation holds the promise of enhancing the adaptability of soft robots when navigating unstructured environments. However, achieving multimodal motions of soft robots remains challenging, as it generally requires variations in the actuation, structures or materials. Two commonly used approaches to realize multimodal motion in soft robots are manipulating multiple actuation sequences and structural reconfigurations [9].

Controlling multiple actuation sequences is the most straightforward method to realize multimodal locomotion. For instance, a soft robot that can form complex trajectories, such as "8" path, is developed by simultaneously controlling three dielectric elastomer actuators [10]. Similarly, diverse gaits in a quadruped soft robot have been realized by controlling multiple pneumatic actuators through a pneumatic circuit [11]. Nonetheless, this method often results in the soft robot's increased size due to the requirements of assembly and the complexity of the control sequences involved.

Structural reconfiguration is another way to enable multimodal motions in soft robots [12], [13], [14], [15], [16]. Many reconfigurable structures have been developed and employed to realize multimodal motions, including origami [17], kirigami [18], and lattice structures [19], [20], [21], [22]. For example, a deformable wheel robots can navigate over gaps by altering the origami wheel's diameters [23]. A shape-changing soft robots can achieve locomotion over a flat and inclined surface by utilizing the shape change during inflation and deflation [24]. An electric-driven soft robot that can realize immediate and reversible forward, backward, and circular direction changes during fast movement has been developed based on a chiral lattice foot design [9].

Bistable structures with the ability to transit between two stable states have been adopted in biological organisms and offered a new design concept to realize multimodal motions [21], [25], [26]. For example, the flytrap leaves adopt a bistable seashell-like form, which quickly changes their curvatures from an inward state before feeding to a close state to engulf insects [17]. Bistable structural design principles span dimensions from 1-D to 3-D, including constrained beams, curved plates, dome shells, deformable origami, and kirigami [21], [27], [28], [29], [30]. Among them, kirigami patterns offer particular versatility by not only enabling bistability, but also enhancing the degree of freedom for shape morphing via introducing well-designed cuts [31], [32].

Manuscript received 26 September 2023; revised 17 January 2024; accepted 12 March 2024. Date of publication 8 April 2024; date of current version 17 December 2024. Recommended by Technical Editor R. Carloni and Senior Editor M. Indri. This work was supported by the National Key Research and Development Program of China under Grant 2022YFB4700900 and in part by the National Natural Science Foundation of China under Grant 52275025. *(Corresponding author: Dong Wang.)*

The authors are with the State Key Laboratory of Mechanical System and Vibration, School of Mechanical Engineering, and the Meta Robotics Institute, Shanghai Jiao Tong University, Shanghai 200240, China (e-mail: ruichenwang_sjtu@sjtu.edu.cn; wangjq_sjtu@sjtu.edu.cn; zzxiao@sjtu.edu.cn; wang_dong@sjtu.edu.cn).

This article has supplementary material provided by the authors and color versions of one or more figures available at https://doi.org/10.1109/TMECH.2024.3379979.

Digital Object Identifier 10.1109/TMECH.2024.3379979

A reversible transition between different states is required for the bistable structures to enhance the independent and autonomous functionality of the soft robot. Hard magnetic soft materials [33], [34], [35], [36], [37], which embed hard magnetic particles (e.g., NdFeB alloys) in a soft polymer matrix (e.g., silicone rubber or gel), offer an avenue for achieving controllable and repetitive actuations [38], [39], [40], [41], [42]. Through magnetization design and magnetic field control, Hu et al. [43] developed millimeter-scale robots that exhibit a range of multimodal movements, including swimming both within and on the surface of liquids, rolling, and walking on solid surfaces, and crawling within narrow tunnels. Wang et al. [44] designed an insect-scale magnetoelastic robot capable of controllable jumping, adaptive amphibious locomotion, and performing tasks with integrated functional modules. Integrating bistable structures and hard magnetic soft materials provide a promising way to realize multimodal motions of soft robots, yet seldom reported. In our previous work [36], we have developed a type of kirigami soft robot that exhibits programmable locomotion under magnetic actuations. However, the magnetic-driven bistability has not been systematically studied.

In this article, we have integrated bistable structures and hard magnetic soft materials to develop untethered soft robots exhibiting programmable multimodal motion under the actuation of magnetic fields. We have adopted a narrow perforated kirigami pattern to introduce bistability. The soft robot comprises perforated kirigami patterns with embedded hard magnetic disks on each face. The hard magnetic disks enable localized magnetic actuations, while the kirigami patterns facilitate shape morphing and snap-through bistability. By manipulating the external magnetic field, the soft robots not only undergo rapid transitions between different stable states but also exhibit distinct motions at each state, owing to variations in their geometric configurations and magnetization orientations. We have developed a theoretical model to quantitatively investigate the bistable transition behaviors, validated by finite-element simulations and experiments. Experimental results demonstrate the versatility of the bistable soft robots, including following "L"-shaped trajectories, displaying amphibious behaviors, and serving as recycle stents. The proposed bistable kirigami design and hard-magnetic driven methods open up possibilities for developing next-generation autonomous soft robots.

The main contribution of this work can be summarized as follows.

1) We have integrated kirigami structures and hard-magnetic soft materials to develop untethered bistable soft robots, which exhibit multimodal motions under magnetic actuations.
2) We have developed a theoretical model based on the energy method to study the formation of bistability and the effects of geometric parameters.
3) The kirigami soft robots demonstrate multifunctions, such as moving along complex trajectories, amphibious behaviors, recycling stents, and logic patterns, by virtue of the bistability.

The rest of this article is organized as follows. We first present the structural design of the bistable kirigami in Section II, followed by the development of the analytical model in Section III. The bistability is then validated by experiments and finite-element simulations in Section IV. Multimodal motions are demonstrated in Section V, followed by applications in Section VI. Finally, Section VII concludes this article.

II. Bistable Design for Magnetic Actuation

A. Structural Design and Fabrication

A periodic kirigami pattern formed by an orthogonal slit is used [see Fig. 1(a)]. Each kirigami unit contains four squares connected by hinges. The hinges enable the in-plane and out-of-plane rotations of the squares. Four hard-magnetic disks with predefined orientations are embedded into the center of each square [see Fig. 1(c)]. Closure with beams on both the left and right sides enable the kirigami structure to form a bistable locomotion [see Fig. 1(b)]. The kirigami pattern enables large deformation due to rotation and monostable/bistable transition, while the hard-magnetic disks provide localized magnetic torque for actuation [see Fig. 1(d)].

The substrate of the bistable kirigami is fabricated by perforating a 4-mm-thick sheet of ethylene-vinyl acetate (EVA) using a laser cutter. The magnetic disks are fabricated by mixing 20 vol% hard-magnetic particles (neodymium-iron-boron, NdFeB, $\sim$5 μm in size) into the silicone rubber. This mixture is homogenized by thoroughly stirring [see Fig. 1(b)]. Following this, the magnetic disks are magnetized under an impulse field of approximately 2 (T, resulting in the acquisition of in-plane magnetization, denoted as $\mathbf{M}$. The four circular holes are fabricated using a laser cutter. The four magnetic disks are then put in circular holes with predefined orientations and bonded using silicone adhesive.

B. Magnetic Actuation

When an external field is applied (labeled as $\mathbf{B}$), the magnetic units tend to align their directions with this applied field, generating magnetic torque $\mathbf{T}=V(\mathbf{M}\times\mathbf{B})$ [45]. This torque subsequently induces deformation in the kirigami structures. Here, V represents the volume of an individual hard-magnetic disk. The angle between $\mathbf{M}$ and $\mathbf{B}$ is defined as θ. Two coordinate systems are used: the local coordinate (X, Y, Z) and global coordinate (x, y, z). The dependence of the magnetic torque on θ is given in Fig. 1(d). Here, the magnitude of $\mathbf{M}$ is 1.10×10^5 A/m, $V=0.79$ cm^3, and a magnetic field along the x-direction $B_x=24$ mT is applied. The local coordinate (X, Y, Z) is set along the kirigami soft robot's length, width, and thickness directions, which is mainly used to describe the local magnetization orientation of the magnetic disks. The global coordinate (x, y, z) is used to describe the direction of the applied field and the orientation of the soft robots.

Multiple combinations are possible based on the orientations of the four magnetic disks. In this work, we have chosen two specific patterns because the kirigami soft robots designed with these two patterns exhibit large deformations when subject to a simple magnetic field: 1) symmetric about Y-axis (YS) [see Fig. 1(e)] and 2) symmetric about X-axis (XS) [see Fig. 1(f)]. The magnetization orientations of the magnetic disks are shown in Fig. 1(e) and (f).

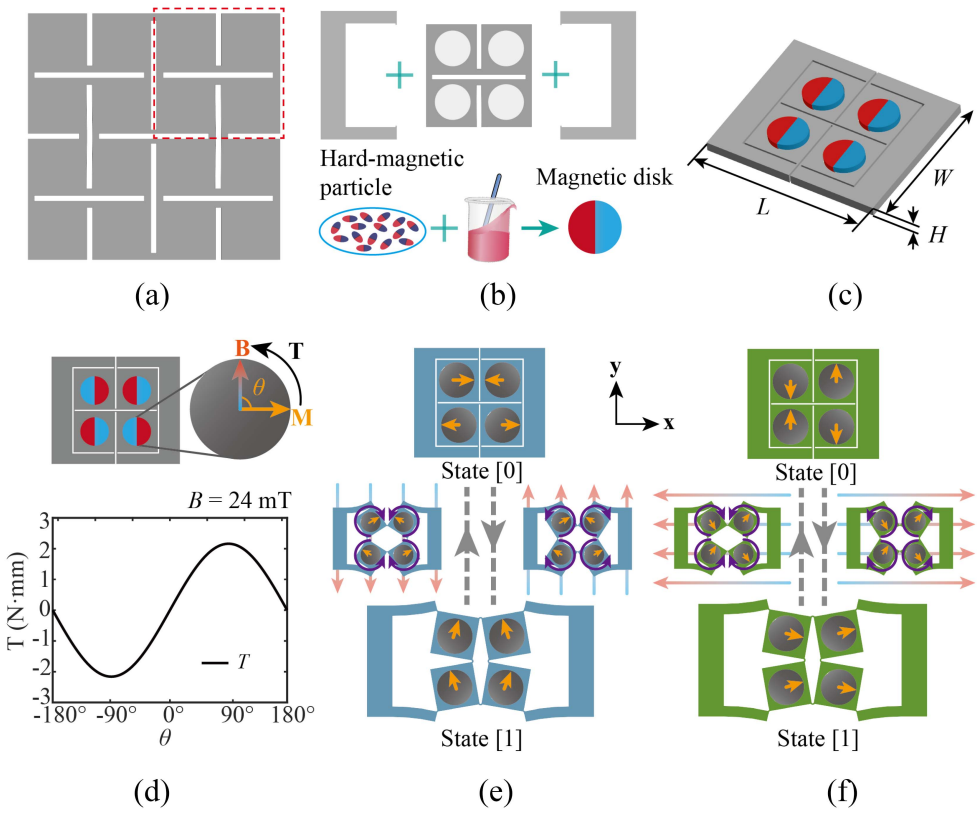

Fig. 1. Bistable kirigami soft robots. (a) Kirigami pattern is formed by orthogonal slit perforations. (b) Substrate of the bistable kirigami is fabricated by perforating a thick sheet of EVA. The magnetic disks are fabricated by mixing hard-magnetic particles into the silicone rubber. (c) Geometric parameters of the kirigami structure. (d) Kirigami soft robots are actuated by localized magnetic torque generated from the hard-magnetic disks. The magnetic torque versus the angle θ between the magnetic field and magnetization directions. (e) and (f) Stable states transition of Y-symmetry (YS) and X-symmetry (XS) soft robots under magnetic actuations.

The transition mechanism is illustrated as follows. We define the initial stable state as State [0] and the deformed stable state as State [1]. For the YS soft robot, the stable State [0] is symmetric about the Y-axis and asymmetric about the X-axis. Therefore, the adjacent facets are subjected to magnetic torques in opposite directions when a $+B_y$ is applied [see Fig. 1(e)]. Hence, the adjacent facets rotate away around the shared joints and the kirigami structure snap-through to stable State [1]. When the magnetic field is removed, State [1] is maintained. As State [1] is symmetric about the Y-axis and asymmetric about the X-axis, all the facets rotate when a $-B_y$ is applied, and the rotation direction is illustrated in Fig. 1(e). The generated magnetic torque then overcome the energy barrier, and the kirigami structure snap-back to State [0]. For the XS soft robots, a similar transition mechanism applies when a B_x is applied. Note that θ changes as the magnetic disk rotates, which changes the applied torque. To ensure enough torque exists to overcome the energy barrier and realize the transition between two stable states, a large magnetic field is needed.

III. Analytical Model

We develop a model based on the energy method to investigate the bistability of the kirigami unit [46]. The kirigami unit contains four elastic beams and eight elastic hinges. These eight hinges can be categorized into two types: four hinges that connect two facets (type I) and four hinges that connect a beam and a facet (type II). We assume that the facets and two side beams remain rigid, as the strains in these regions are relatively small, a hypothesis validated through finite-element simulations later. Hence, the elastic energy of the bistable kirigami structure is the sum of the energy stored in the four elastic beams and eight hinges [47].

A. Elastic Energy of the Beams

The geometric parameters are shown in Fig. 2(a)(i). The kirigami unit has the following dimensions: length L, width W, and height H. Each square within it has a side length of L_x. The length of the elastic beam is $L_e = L_x + L_c$, where L_c is the width of the slit and L_t is the width of the hinge. When the kirigami structure deploys, the square facets undergo rotation, represented by a tilting angle θ_a. The axial strain ε can be calculated as

$$\varepsilon = \frac{2L_x \sin\theta_a}{L}. \tag{1}$$

Both the elastic beams and the hinges bend during the deployment of the kirigami structure. The elastic energy of the deformed beams is calculated first. One end of the elastic beam is anchored, while the other end undergoes a deflection

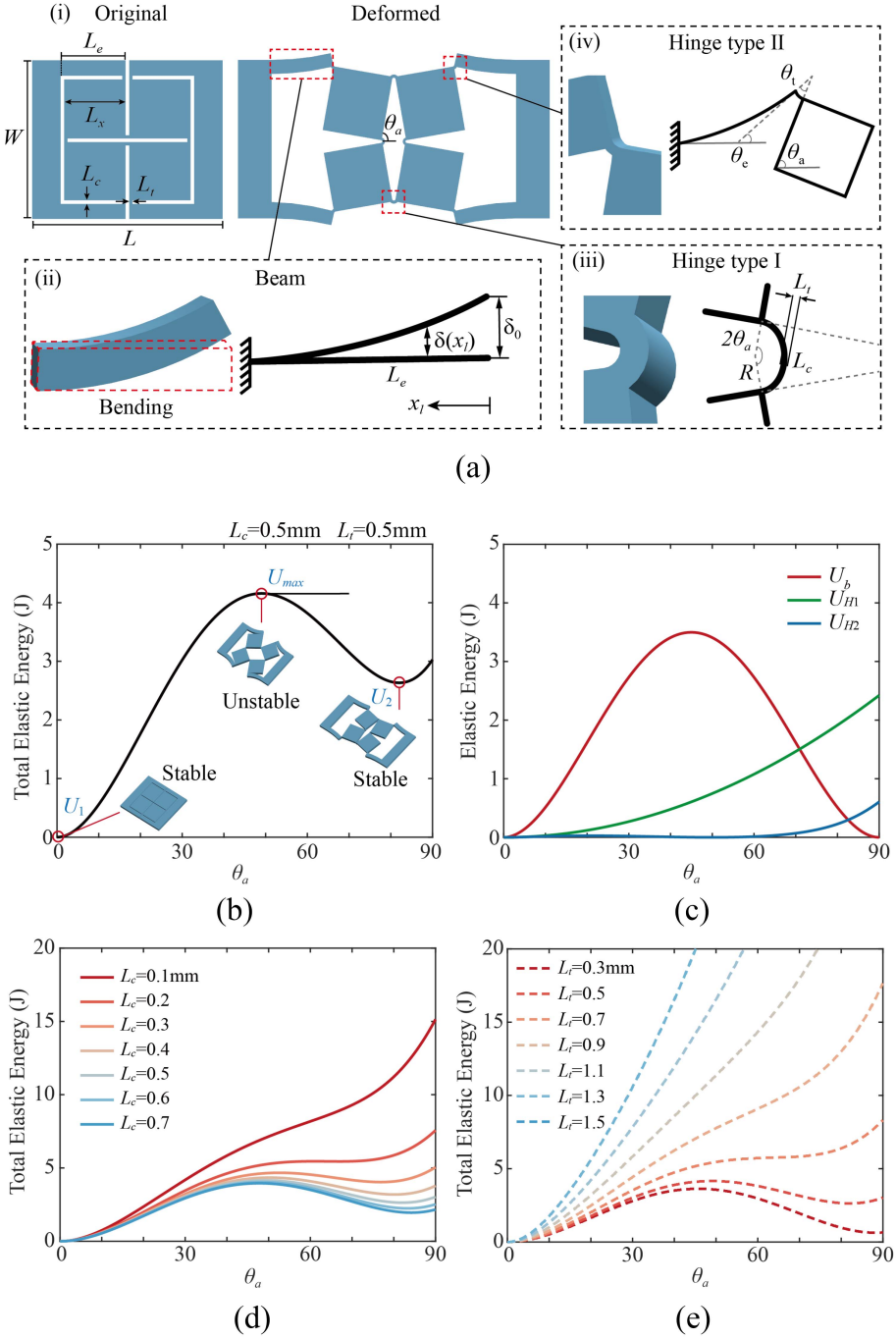

Fig. 2. Analytical model. (a) Geometric parameters of the kirigami structure: length L, width W, height H, width of the slit L_c, and width of the hinge L_t. Each square within it has a side length of L_x. (b) Plots the theoretical total elastic energy curve of a bistable kirigami structure. (c) Plots the dependence of U_b (energy stored in the beams), U_{H1} (the energy stored in hinge type I), and U_{H2} (the energy stored in hinge type II) on θ_a. (d) and (e) Dependence of the total elastic energy on θ_a as L_c and L_t change.

$\delta_0 = L_x(\sin\theta_a + \cos\theta_a - 1)$, as shown in Fig. 2(a)(ii). The equilibrium of moments in the deflected beam can be expressed as

$$M(x_l) = EI\frac{d^2\delta(x_l)}{dx^2} \tag{2}$$

where $M(x_l)$ is the internal moment, $\delta(x_l)$ is the deflection along the beam's length x_l, E is the Young's modulus, and I is the second moment of area of the beam's cross section. The origin of x_l is defined at deflection side. The boundary conditions are $\delta(x_l) = \delta'(x_l) = 0$ at $x_l = L_e$ and $\delta(x_l) = \delta_0$ at $M(x_l)$ and $\delta(x_l)$ can then be calculated as

$$\delta(x_l) = \frac{\delta_0}{2{L_e}^3}{x_l}^3 - \frac{3\delta_0}{2L_e}x_l + \delta_0$$
$$M(x_l) = \frac{3EI\delta_0}{{L_e}^3}x_l. \tag{3}$$

The energy stored in the beam, denoted as U_b is calculated as

$$U_b = \int_0^{L_e} \frac{M(x_l)^2}{2EI} dx_l = \frac{3EI[L_x(\sin\theta_a + \cos\theta_a - 1)]^2}{{L_e}^3}. \quad (4)$$

B. Elastic Energy in Hinge Type I

Hinge type I connects two adjacent facets. The length and width of hinge type I are L_c and L_t. We make the assumption that hinge type I exhibits bending with a constant radius [48], denoted as R [as depicted in Fig. 2(a)(iii)]. The radius R can be calculated as

$$R = \frac{L_c}{2\theta_a}. \quad (5)$$

The elastic energy stored in the elastic hinge can be calculated from the bending strain energy per unit area u_h as [46]

$$u_h = \frac{1}{2}\frac{D}{R^2} \quad (6)$$

where $D = \frac{E{L_t}^3}{12(1-\nu^2)}$ is the bending rigidity and ν is the Poisson's ratio. Hence, the energy stored in hinge type I is

$$U_{H1} = 2\theta_a RH u_h. \quad (7)$$

C. Elastic Energy in Hinge Type II

Hinge type II connects the beam to the facet and undergoes bending as the facet rotates [see Fig. 2(a)(iv)]. The bending angle θ_t of hinge type II is given by

$$\theta_t = \theta_a - \theta_e$$

where $\theta_e = \arctan \delta'(x_l)|_{x_l=0} = \arctan \frac{3\delta_0}{L_e}$ is the slope angle of the beam at $x_l = 0$, calculated using (3). The radius of hinge type II can be calculated as $R_t = L_c/\theta_t$. The elastic energy per unit area stored in the hinge type II is

$$u_{h2} = \frac{1}{2}\frac{D}{{R_t}^2}. \quad (8)$$

Hence, the energy stored in hinge type II is

$$U_{H2} = u_{h2}\theta_t R_t h = \frac{Dh}{2L_c}\left(\theta_a - \arctan\frac{3\delta_0}{L_e}\right)^2. \quad (9)$$

D. Total Elastic Energy

The total elastic energy of the kirigami unit is the sum of the energy stored in the four elastic beams, four hinge type I, and four hinge type II as follows:

$$U_{\text{total}} = 4U_b + 4U_{H1} + 4U_{H2} \quad (10)$$

which can be written explicitly as

$$U_{\text{total}} = 4\left(\frac{3EI[L_x(\sin\theta_a + \cos\theta_a - 1)]^2}{{L_e}^3}\right) + 4\left(2\theta_a RH u_h\right) + 4\left(\frac{Dh}{2L_c}\left(\theta_a - \arctan\frac{3\delta_0}{L_e}\right)^2\right). \quad (11)$$

The bistability property can be analyzed by evaluating the dependence of U_{total} on the rotation angle θ_a.

IV. Bistability Analysis

Fig. 2(b) plots the theoretical total elastic energy curve of a kirigami structure. The geometric parameters are $L_e = 15$ mm, $L_x = 14.6$ mm, $L_c = 0.5$ mm, $L_t = 0.5$ mm, and $H = 6$ mm. The width of the beam is 4 mm. The Young's modulus $E = 840$ MPa and the Poisson's ratio $\nu = 0.38$. The elastic energy curve reveals that the kirigami structure is bistable. As θ_a increases, U_{total} increases and reaches its maximum at $\theta_a = 49°$. Subsequently, U_{total} decreases and achieves a local minimum U_2 at $\theta_a = 82°$, which is the second stable state, State [1].

To understand the mechanism of the bistability, Fig. 2(c) plots the dependence of U_b, U_{H1}, and U_{H2} on θ_a. Both U_{H1} and U_{H2} exhibit a monotonic increase with θ_a. However, U_b increases and reaches its maximum at $\theta_a = 45°$ first, and then, decreases. The nonmonotonic behavior of U_b with θ_a causes the bistability.

To investigate the influence of geometric parameters on bistability, Fig. 2(d) plots the change U_{total} with θ_a for different L_c, ranging from 0.1 to 0.7 mm. The other geometric and material parameters are the same as the kirigami structure in Fig. 2(b). We determine a critical L_c of 0.19 mm by setting the derivative of U_{total} with respect to θ_a as 0. For L_c exceeding 0.19 mm, a local minimum of U_{total} exists between $\theta_a = \sim 70°$ and $\sim 90°$, indicative of bistability. Conversely, when L_c is less than 0.19 mm, the energy increases monotonically with θ_a, indicating a monostable state. The effect of L_t is also explored, as shown in Fig. 2(e), which depicts the dependence of U_{total} on θ_a for varying L_t (ranging from 0.3 to 1.5 mm). The critical L_t is calculated as 0.7 mm. We observe that the structure is monostable when L_t exceeds 0.7 mm, and bistable when L_t falls below 0.7 mm.

We then experimentally validate the bistability behaviors of structures (Movie 1). Fig. 3(a) presents the uniaxial tensile force–strain curves of two kirigami structures, one with $L_t = 0.5$ mm (shown in blue) and the other with $L_t = 1.5$ mm (shown in red). The material and geometric parameters are the same as the structure shown in Fig. 2(b). For the kirigami structure with $L_t = 0.5$ mm, the tensile force initially increases and reaches its maximum, after which it drops rapidly to a negative value due to the snap-through behavior. Subsequently, the force increases fast after State [1], as the deformation of the kirigami structure is stretch dominated. In contrast, the kirigami structure with $L_t = 1.5$ mm exhibits a monotonic increasing tensile force. The experimental results agree well with the theoretical predictions.

Fig. 3(b) and (c) displays snapshots from both experiments and finite-element analysis at the three distinct states labeled as I–III. In the FE analysis, the ABAQUS Standard Implicit Dynamics solver is employed. The Mooney–Rivlin hyperelastic material is used with $C_{10} = -0.094$ MPa and $C_{01} = 0.83$ MPa. Meshing is performed using ten-node quadratic tetrahedron elements with hybrid formulation (C3D20H). Boundary conditions

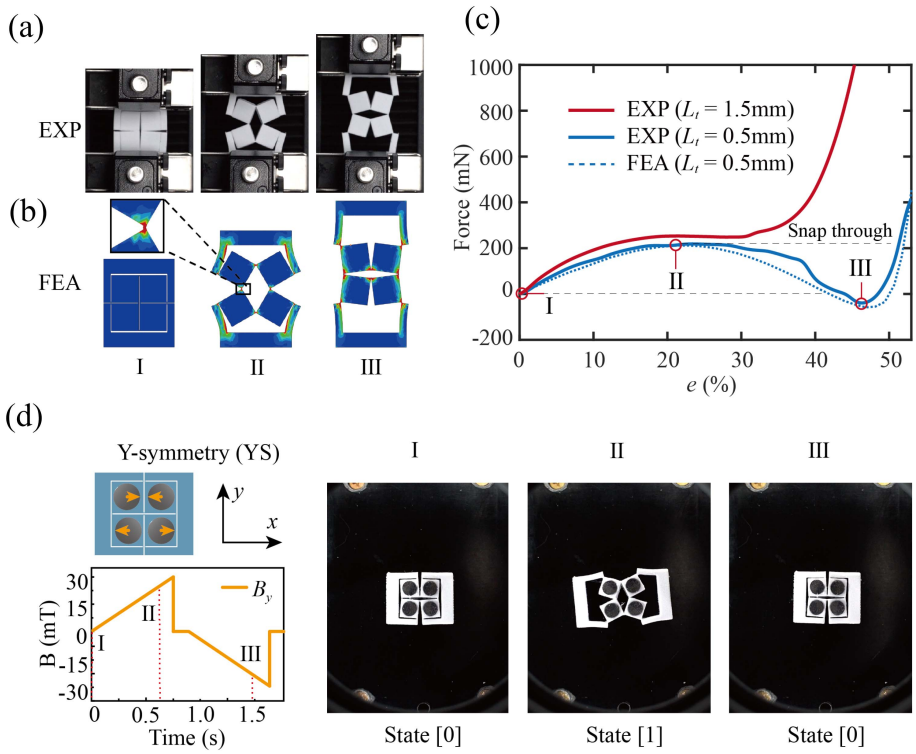

Fig. 3. Finite-element analysis and experimental test of the bistability. (a) Uniaxial tensile tests of the bistable kirigami. (b) Snapshots from finite-element simulations. (c) Experimental and finite-element simulated force–strain curves of kirigami structures. (d) Bistability of a YS kirigami soft robot under magnetic actuation.

are the same as experiments. The FE simulated force–strain curve agrees well with the experimental results. Moreover, the principal strain maps at States I–III illustrate that strain primarily localizes at the hinges and constrained beams, with negligible deformation observed in the rest of the structure. It validates the assumptions made in the theoretical model that the elastic energy stored in the facets and the side beams can be ignored.

We test the bistability of the kirigami soft robots (Movie 2). A YS kirigami soft robot is used. Fig. 3(d) illustrates the magnetization orientations of the four magnetic disks. The variation of the magnetic field B_y with time is depicted. A ramp B_y is applied first, increasing from 0 to 30 mT in a time interval 0.75 s. As B_y increases, the kirigami soft robot undergoes deployment and transitions from State [0] to [1]. The kirigami soft robot remains at State [1] as B_y returns to zero, indicating State [1] is a stable state. Subsequently, the application of a negative ramp B_y, decreasing from 0 to -30 mT, induces a rapid snap-back of the kirigami soft robot to its initial State [0].

V. Dynamic Motions

The bistable kirigami soft robot can transit between two stable states reversibly under a large B_x. In this section, we demonstrate that the kirigami soft robot can realize direction locomotion at State [0] under a combined B_y and B_z, and a rigid rotation at State [1] under an in-plane magnetic field. By combining the distinct motions at States [0] and [1], and the transition between the two states, various multimodal motions can be generated.

A. Directional Locomotion at State [0]

The kirigami design enables the directional motion of the robot at State [0] when a combined B_y and B_z are applied simultaneously (Movie 2). To investigate this, we conduct experiments using periodic square waves with a 2-Hz frequency, employing both zero and π phase differences. Fig. 4(a) depicts the motion of the YS kirigami soft robot. We apply a combined magnetic field consisting of B_y and B_z components. The results demonstrate that the soft robot moves toward the $+Y$ direction when the phase difference between B_y and B_z is 0, and toward the $-Y$ direction when the phase difference is π. When only a single periodic B_y and B_z field is applied, the motion remains symmetric but limited to the soft robot's original position. However, the combination of B_y and B_z fields generates a synergistic effect, resulting in directional motion. Fig. 4(a)(ii) illustrates the trajectory of the central hinge marked with blue dots. Furthermore, Fig. 4(a)(iii) presents finite-element analysis deformation shapes under negative (Mode 1) and positive (Mode 2) B_y and B_z fields.

B. Rigid Rotation at State [1]

The soft robot exhibits a rigid rotation at State [1], enabled by the nontrial net magnetization and the large effective modulus. Unlike the zero net magnetization in State [0], State [1] of the kirigami soft robot possesses a nontrivial net magnetization. The net magnetization in State [1] is illustrated in Fig. 4(b)(i), pointing toward the $+Y$ direction. The net magnetization is the vector sum of the magnetizations of the four magnetic disks. Moreover, the effective modulus of the kirigami structures at

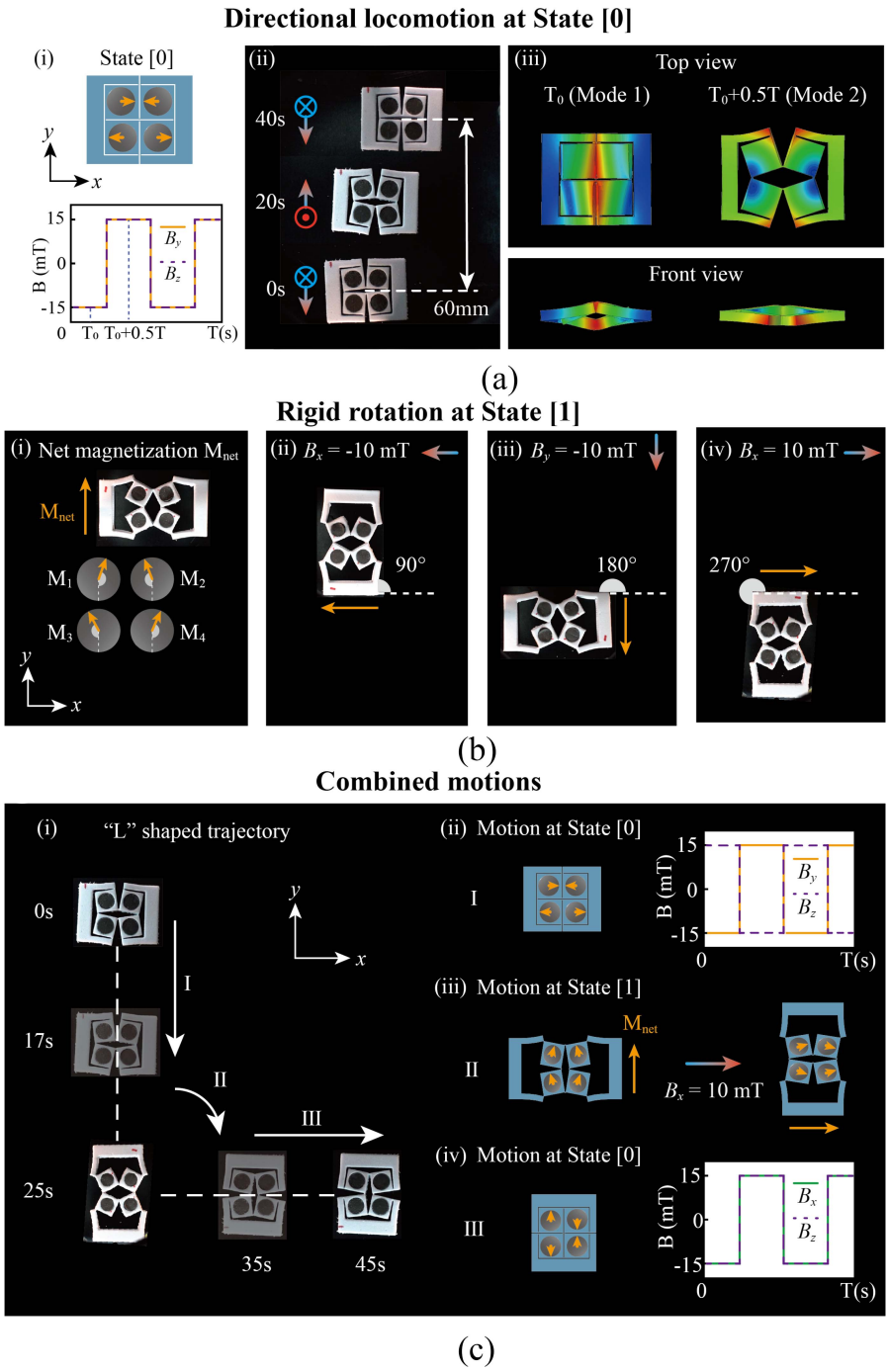

Fig. 4. Dynamic motions of the bistable kirigami soft robot. (a) YS kirigami soft robot shows directional locomotion at stable State [0] under combined B_y and B_z. (b) YS kirigami soft robot shows a rigid rotation of YS kirigami at stable State [1] under in-plane magnetic actuation. (c) YS kirigami soft robot navigates along an "L" path utilizing its multimodal motions.

State [1] is 42 times larger than that at State [0]. The effective modulus is obtained by differentiating the U_{total} with respect to Δx twice. The nontrial net magnetization and the large effective modulus combined allows for rigid body motion under a simple magnetic field, as the net magnetization tends to align with the external magnetic field. For instance, when an external magnetic field with $B_x = -10$ mT, $B_y = -10$ mT, and $B_x = 10$ mT is sequentially applied, the kirigami soft robot undergoes continuous rotations [see Fig. 4(b)(ii)–(iv)] (Movie 2). Using this method, the kirigami soft robot can achieve 360° rotations in State [1] by controlling the magnetic field.

C. Combined Motions

The unique motions in the two stable states, combining with the bistable transition, enable versatile locomotion in unstructured environments. We demonstrate the capabilities of a kirigami soft robot to navigate along an "L" path utilizing its

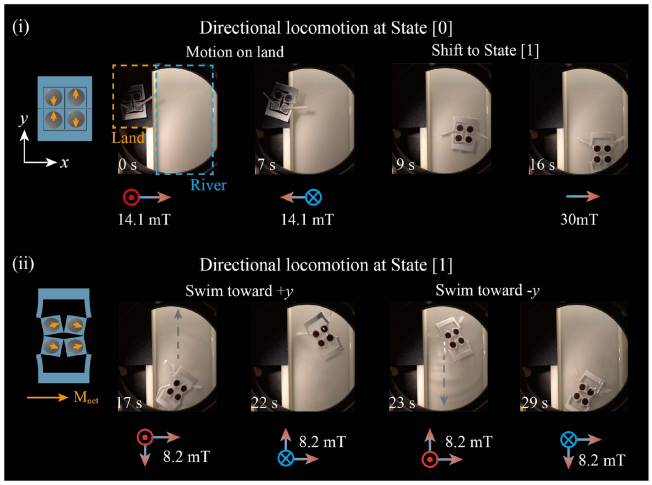

Fig. 5. Amphibious bistable soft robot capable of moving in both terrestrial and aquatic environments.

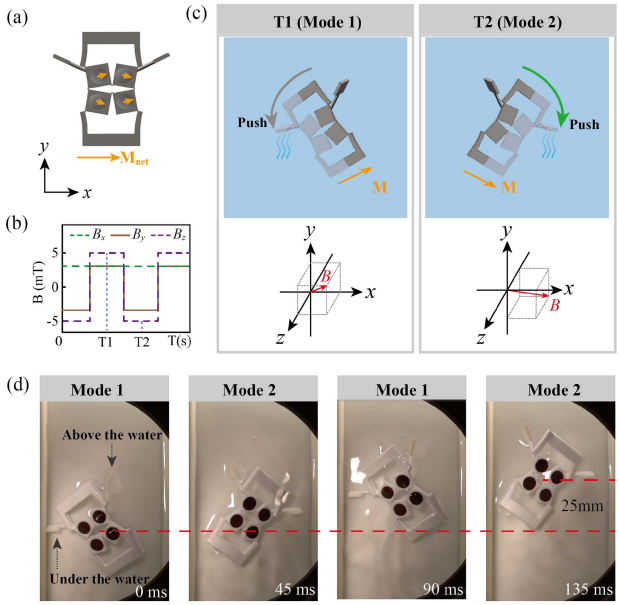

Fig. 6. Gait analysis of amphibious soft robots. (a) Net magnetization of the amphibious soft robot. (b) Applied magnetic fields. (c) Motion of the amphibious soft robot exhibits two distinct modes. (d) Soft robot could swim in the $+y$ direction, resembling freestyle swimming.

multimodal motion [see Fig. 4(c)(i)] (Movie 3). Initially, under a combined periodic B_y and B_z with a phase difference π, the soft robot moves downward attributes to the directional locomotion at State [0] [see Fig. 4(c)(ii)]. Upon reaching the turning point, an external field of $+B_y = 24$ mT is applied and the soft robot transits from State [0] to [1]. Subsequently, a $+B_x = 10$ mT field is employed to rotate the soft robot clockwise by 90° [see Fig. 4(c)(iii)]. After the rigid rotation, the soft robot returns to the initial State [0] when a $-B_x = -24$ mT field is applied. The soft robot then exhibits direction locomotion to the left when a combined B_x and B_z field is applied [see Fig. 4(c)(iv)].

VI. Application Prospects

In this section, the bistable property of the kirigami soft robots have been used to display amphibious behaviors, energy release, serving as recycling stents, and logic patterns. Amphibious capability is an essential survival strategy. Consider sea lions and sea turtles, which adeptly employ their front flippers both for swimming and for supporting their large bodies when traversing land, functioning as quadrupeds. The transition between these modes of motion is key to their success. We have developed an amphibious bistable soft robot capable of moving in both terrestrial and aquatic environments. This amphibious soft robot features two paddles affixed beneath the left magnetic disks to ensure flexibility (Movie 4). When a B_x magnetic field is applied, the magnetic disks of a YS kirigami soft robot rotate around the hinges, and the kirigami structure transits to another stable state. As illustrated in Fig. 5(i), the bistable kirigami soft robot moves from the ground to the water environment under the influence of a combined square-wave B_x and B_z magnetic field. Upon entering the pool, a positive B_z is applied, and the kirigami structure transits to State [1]. The paddles also adjust their position in response to the magnetic disk rotation. With a phase difference of 0, the kirigami soft robot swims toward the $+y$ direction, while a phase difference of π prompts it to swim in the $-y$ direction [see Fig. 5(ii)].

Fig. 6 shows the gait analysis of amphibious soft robots during swimming. The soft robot in State [1] has a nonzero net magnetization, pointing in the right direction [see Fig. 6(a)]. Fig. 6(b) gives the applied external magnetic field when the soft robot swims to the positive y-direction. A constant $B_x = 3$ mT is applied, while ± 3 mT and ± 5 mT square waves are applied to B_y and B_z, respectively. When an external magnetic field is applied, the net magnetization of the soft robot tends to align with the external magnetic field, resulting in the two distinct modes [see Fig. 6(c)]. In Mode 1 (at time T1), the positive B_z causes the left part of the soft robot to sink and B_x and B_y contribute to the soft robot's counterclockwise rotation in the x–y plane. Consequently, the left paddle propels the soft robot forward. Similarly, the right part sinks due to the negative B_z, and the soft robot rotates clockwise in Mode 2 (at time T2). This motion results in the right paddle propelling the soft robot forward. As a result, the soft robot could swim toward the $+y$ direction, resembling freestyle swimming [see Fig. 6(d)]. The soft robot can swim 25 mm in 135 ms.

A characteristic of bistable transition is the energy release. The energy can be quickly released after overcoming the energy barrier. As demonstrated in Fig. 7(a), a bistable kirigami soft robot (25 mm in length and 0.5 g in weight) is capable of pushing a large cylinder (25 mm in diameter and 3.5 g in weight) under the influence of $+B_y$ (Movie 5). The distribution of the magnetic disk and the applied external magnetic field are depicted [see Fig. 7(a)(i)]. The soft robot effectively converts the released energy into kinetic energy, pushing the large cylinder out by 18 mm.

This energy release property is further utilized in Fig. 7(b), where a YS kirigami soft robot functions as a recycling stent, expanding the "vessel wall" (Movie 5). Initially, the soft robot, in State [0], moves toward the $+Y$ direction under periodic B_y and

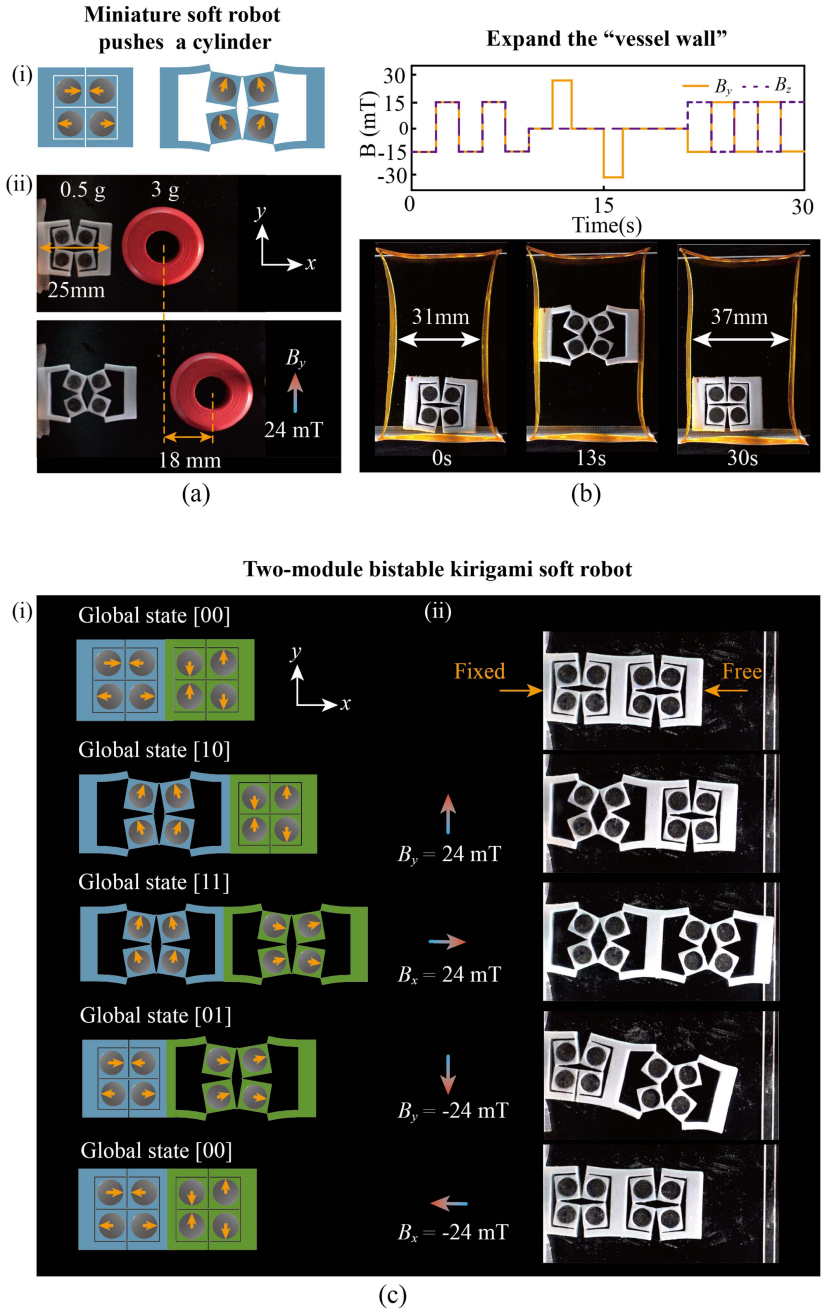

Fig. 7. Application prospects of the bistable kirigami soft robots. (a) Miniature bistable kirigami soft robot (length is 25 mm and weight is 0.5 g) pushes a large cylinder (diameter is 25 mm and weight is 3.5 g). (b) YS kirigami soft robot functions as a recycling stent, expanding the "vessel wall." (c) TTwo-module kirigami soft robot (YS+XS) realizes sequential actuations.

B_z fields with a phase difference of 0. Upon reaching a narrow position (31 mm in width), the soft robot transitions from State [0] to [1] by applying $B_y = 24$ mT. During this process, the soft robot releases energy, pushing the "vessel wall." Unlike conventional stents that remain in the vessel, the kirigami soft robot can transition back to State [0] by applying $B_y = -24$ mT and return to its original position. Notably, the width of the "vessel wall" increases to 37 mm.

Multiple bistable kirigami soft robots can be combined to realize sequential actuations and show logic patterns (Movie 5). Fig. 7(c) shows two-module bistable kirigami soft robots (YS+XS). Here, the global states are defined by a binary code [ij] with *i* and *j* denoting states 0 and 1 of the right and left bistable kirigami, respectively. Through controlling the magnetic field's intensity and direction, we can interchange between the four global states. When $B_y = 24$ mT is applied, the YS module transits to State [1], while the XS module remains locked because the applied magnetic field is parallel to the magnetization direction, resulting in global state [10] [see Fig. 7(c)(i)]. Subsequently, upon the application of a strong B_x field, the XS module transits to State [1], while the YS module is locked due to the counterclockwise torque exerted by its four magnetic

disks, leading to a new global state [11]. Then, applying a $-B_y$ magnetic field can rotate the YS module back to stable State [0], transitioning to global State [01]. Finally, the XS module rotates to stable State [0] under $-B_x$, resulting in global state [00] [see Fig. 7(c)(ii)].

VII. Conclusion

Magnetic soft robots possess the advantages of rapid, reversible, and untethered responses, offering potential applications in various fields. However, the multimodal motion of these robots is hindered by the geometric constraint of the bulk shape and the fixed magnetization orientations. Kirigami can release the geometric constraint by introducing cuts to guide buckling/folding processes, which can induce planar or nonplanar shape transformations. The kirigami facets also serve as platforms for embedding components compatible with magnetic functional materials. Moreover, bistability can be enabled by rational cut design. The shape and magnetization differences in different stable states allow for multimodal motion. In addition, the bistable transition generates a large output force quickly due to the abrupt release of accumulated strain energy. Therefore, the bistable kirigami structure is adopted to design magnetic soft robots.

The soft robot exhibits diverse and multimodal motions, showing promising applications in medical settings. However, the working range of the soft robot is limited by the actuation system. Improvement in fabrication and actuation techniques may overcome this challenge. 3-D printing technology provides a way to fabricate miniature kirigami structures. Leveraging digital light processing 3-D printing for the matrix material and magnetic direct ink writing for the magnetic components enables the development of miniature kirigami soft robots. Introducing a parallel-mobile-coil system, in which coils are intricately embedded within the structure of the parallel mechanism and capable of 3-D movement, offers an alternative means of generating a controllable magnetic field [49]. By combining the miniature soft robot and parallel-mobile-coil system, medical applications become feasible, including medicine delivery, physiologic monitoring, or vascular interventional treatment. For example, the facets of the kirigami structure provide platforms for integrating sensors, enabling continuous monitoring of physiologic characteristics of the stomach, such as pH, viscoelasticity, and biomarkers for disease diagnosis [50]. The soft robot can be used for human vascular interventional trial surgery treatment. With its excellent mobility and bistability, it could reach the location of the vascular obstruction and act as a vascular stent or release drugs.

In this work, we develop untethered soft robots capable of programmable multimodal motions by integrating bistable kirigami structures and hard magnetic actuations. The soft robot comprises of a narrow perforated kirigami pattern with embedded hard magnetic disks on each face. The hard magnetic disks enable localized magnetic actuations, while the kirigami patterns facilitate shape morphing and snap-through bistability. By manipulating the external magnetic field, the soft robots not only undergo rapid transitions between stable States [0] and [1] but also exhibit distinct motions at each state, owing to variations in their geometric configurations and magnetization orientations. To understand the bistable transition behaviors, we develop a theoretical model based on the energy method, which is subsequently validated through finite-element analysis and experiments. Critical geometric parameters for the monostable/bistable transition are calculated. The kirigami pattern also enables the combination of multiple units. Experimental results demonstrate the versatility of the bistable soft robots. In particular, we design soft robots capable of following "L"-shaped trajectories, displaying amphibious behaviors, and serving as recycle stents, by virtue of the bistability. The proposed bistable kirigami design and hard-magnetic driven methods open up possibilities for developing next-generation autonomous soft robots.

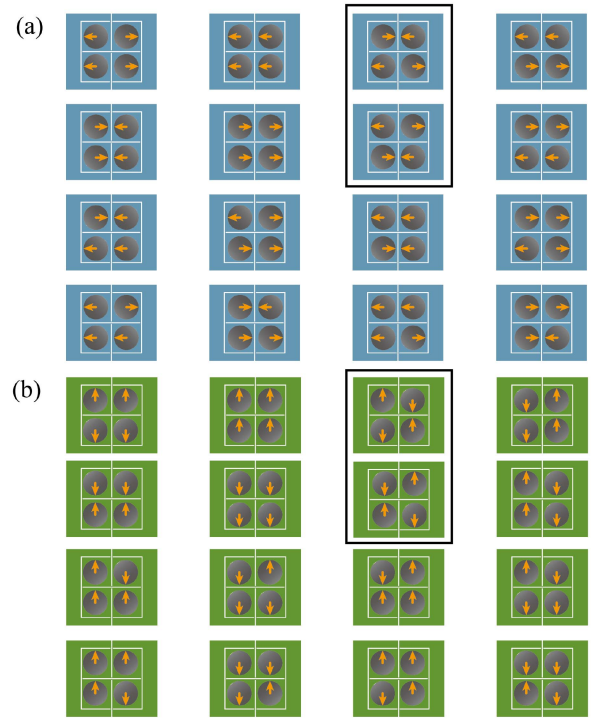

Fig. 8. Possible arrangements of the four magnetic disks in a kirigami soft robot. The patterns in (a) and (b) are *Y*-symmetry and *X*-symmetry, respectively. The patterns in the black circles are chosen in the experiments because they transit from State [0] to State [1] when a $\pm B_y$ or $\pm B_x$ is applied.

Appendix A
Arrangement of Magnetic Disks

Fig. 8 shows 32 different permutations of the magnetization array of the four magnetic disks. The magnetization of each magnetic disk is set along the *Y*-axis or *X*-axis. The patterns in (a) and (b) are *Y*-symmetry and *X*-symmetry, respectively. The patterns in the black circles are chosen in the experiments because they can transit from State [0] to State [1] when a $+B_y$ or $+B_x$ is applied. The patterns in the same circles belong to the same category and exhibit the same bistability, as they are the same pattern by rotating 180° with respect to the center.

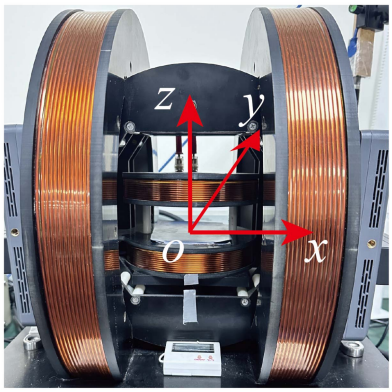

Fig. 9. Magnetic actuation system with Helmholtz coils.

A customized 3-D Helmholtz coil device is designed to produce uniform magnetic fields consisting of three pairs of orthogonal Helmholtz coils (see Fig. 9). The workspace dimensions are 120 × 80 × 40 mm. Each Helmholtz coil can generate a uniform magnetic field along the x, y, and z directions, with maximum magnitudes of 30, 25, and 15 mT, respectively. The strength of these magnetic fields is proportional to the current supplied to the Helmholtz coils. The magnitude and shapes of the current are controlled by a waveform generator, allowing for the generation of various waveforms such as constant value, sinusoidal, and square waves. Independent control of the current applied to each Helmholtz coil facilitates the superimposition of magnetic fields. This setup provides precise control over the magnetic field's strength, type, and orientation.

REFERENCES

[1] H.-T. Lin, G. G. Leisk, and B. Trimmer, "GoQBot: A caterpillar-inspired soft-bodied rolling robot," *Bioinspiration Biomimetics*, vol. 6, no. 2, 2011, Art. no. 026007.

[2] D. Savile, "Adaptive evolution in the avian wing," *Evolution*, vol. 11, pp. 212–224, 1957.

[3] Z. Xie et al., "Octopus arm-inspired tapered soft actuators with suckers for improved grasping," *Soft Robot.*, vol. 7, no. 5, pp. 639–648, 2020.

[4] Z. Gao, Q. Shi, T. Fukuda, C. Li, and Q. Huang, "An overview of biomimetic robots with animal behaviors," *Neurocomputing*, vol. 332, pp. 339–350, 2019.

[5] Z. Wang, S. Guo, J. Guo, Q. Fu, L. Zheng, and T. Tamiya, "Selective motion control of a novel magnetic-driven minirobot with targeted drug sustained-release function," *IEEE/ASME Trans. Mechatron.*, vol. 27, no. 1, pp. 336–347, Feb. 2022.

[6] D. Wang et al., "Soft actuators and robots enabled by additive manufacturing," *Annu. Rev. Control, Robot., Auton. Syst.*, vol. 6, pp. 31–63, 2023.

[7] C. Jiang, D. Wang, B. Zhao, Z. Liao, and G. Gu, "Modeling and inverse design of bio-inspired multi-segment pneu-net soft manipulators for 3D trajectory motion," *Appl. Phys. Rev.*, vol. 8, no. 4, 2021, Art. no. 041416.

[8] R. Chen, Z. Zhang, J. Guo, F. Liu, J. Leng, and J. Rossiter, "Variable stiffness electroadhesion and compliant electroadhesive grippers," *Soft Robot.*, vol. 9, no. 6, pp. 1074–1082, 2022.

[9] D. Wang et al., "Dexterous electrical-driven soft robots with reconfigurable chiral-lattice foot design," *Nature Commun.*, vol. 14, no. 1, 2023, Art. no. 5067.

[10] X. Ji et al., "An autonomous untethered fast soft robotic insect driven by low-voltage dielectric elastomer actuators," *Sci. Robot.*, vol. 4, no. 37, 2019, Art. no. eaaz6451.

[11] D. Drotman, S. Jadhav, D. Sharp, C. Chan, and M. T. Tolley, "Electronics-free pneumatic circuits for controlling soft-legged robots," *Sci. Robot.*, vol. 6, no. 51, 2021, Art. no. eaay2627.

[12] W. Pang et al., "A soft microrobot with highly deformable 3D actuators for climbing and transitioning complex surfaces," *Proc. Nat. Acad. Sci. USA*, vol. 119, no. 49, 2022, Art. no. e2215028119.

[13] N. D. Thorat et al., "Physically stimulated nanotheranostics for next generation cancer therapy: Focus on magnetic and light stimulations," *Appl. Phys. Rev.*, vol. 6, no. 4, 2019, Art. no. 041306.

[14] Z. Li, N. V. Myung, and Y. Yin, "Light-powered soft steam engines for self-adaptive oscillation and biomimetic swimming," *Sci. Robot.*, vol. 6, no. 61, 2021, Art. no. eabi4523.

[15] Y. Kim, J. van den Berg, and A. J. Crosby, "Autonomous snapping and jumping polymer gels," *Nature Mater.*, vol. 20, no. 12, pp. 1695–1701, 2021.

[16] Q. Ge et al., "3D printing of highly stretchable hydrogel with diverse UV curable polymers," *Sci. Adv.*, vol. 7, no. 2, 2021, Art. no. eaba4261.

[17] Q. Ze et al., "Spinning-enabled wireless amphibious origami millirobot," *Nature Commun.*, vol. 13, no. 1, 2022, Art. no. 3118.

[18] Y. Tang, Y. Li, Y. Hong, S. Yang, and J. Yin, "Programmable active kirigami metasheets with more freedom of actuation," *Proc. Nat. Acad. Sci. USA*, vol. 116, no. 52, pp. 26407–26413, 2019.

[19] D. Wang, L. Dong, and G. Gu, "3D printed fractal metamaterials with tunable mechanical properties and shape reconfiguration," *Adv. Funct. Mater.*, vol. 33, no. 1, 2023, Art. no. 2208849.

[20] L. Dong, J. Wang, and D. Wang, "Modeling and design of three-dimensional voxel printed lattice metamaterials," *Additive Manuf.*, vol. 69, 2023, Art. no. 103532.

[21] Y. Chi, Y. Li, Y. Zhao, Y. Hong, Y. Tang, and J. Yin, "Bistable and multistable actuators for soft robots: Structures, materials, and functionalities," *Adv. Mater.*, vol. 34, no. 19, 2022, Art. no. 2110384.

[22] D. Wang, C. Jiang, and G. Gu, "Modeling and design of lattice-reinforced pneumatic soft robots," *IEEE Trans. Robot.*, vol. 40, pp. 606–623, 2024.

[23] D.-Y. Lee, G.-P. Jung, M.-K. Sin, S.-H. Ahn, and K.-J. Cho, "Deformable wheel robot based on origami structure," in *Proc. IEEE Int. Conf. Robot. Automat.*, 2013, pp. 5612–5617.

[24] D. S. Shah, J. P. Powers, L. G. Tilton, S. Kriegman, J. Bongard, and R. Kramer-Bottiglio, "A soft robot that adapts to environments through shape change," *Nature Mach. Intell.*, vol. 3, no. 1, pp. 51–59, 2021.

[25] T. Chen, J. Mueller, and K. Shea, "Integrated design and simulation of tunable, multi-state structures fabricated monolithically with multi-material 3D printing," *Sci. Rep.*, vol. 7, no. 1, 2017, Art. no. 45671.

[26] C. Y. Li, D. Jiao, X. P. Hao, W. Hong, Q. Zheng, and Z. L. Wu, "Bistable joints enable the morphing of hydrogel sheets with multistable configurations," *Adv. Mater.*, vol. 35, no. 15, 2023, Art. no. 2211802.

[27] Y. Cho et al., "Engineering the shape and structure of materials by fractal cut," *Proc. Nat. Acad. Sci. USA*, vol. 111, no. 49, pp. 17390–17395, 2014.

[28] Y. Sun, W. Ye, Y. Chen, W. Fan, J. Feng, and P. Sareh, "Geometric design classification of kirigami-inspired metastructures and metamaterials," *Structures*, vol. 33, pp. 3633–3643, 2021.

[29] J. Tao, H. Khosravi, V. Deshpande, and S. Li, "Engineering by cuts: How kirigami principle enables unique mechanical properties and functionalities," *Adv. Sci.*, vol. 10, no. 1, 2023, Art. no. 2204733.

[30] A. Rafsanjani, L. Jin, B. Deng, and K. Bertoldi, "Propagation of pop ups in kirigami shells," *Proc. Nat. Acad. Sci. USA*, vol. 116, no. 17, pp. 8200–8205, 2019.

[31] Y. Yang, A. Vallecchi, E. Shamonina, C. J. Stevens, and Z. You, "A new class of transformable kirigami metamaterials for reconfigurable electromagnetic systems," *Sci. Rep.*, vol. 13, no. 1, 2023, Art. no. 1219.

[32] T. van Manen, S. Janbaz, M. Ganjian, and A. A. Zadpoor, "Kirigami-enabled self-folding origami," *Mater. Today*, vol. 32, pp. 59–67, 2020.

[33] T. Jiralerspong, G. Bae, J.-H. Lee, and S.-K. Kim, "Wireless control of two-and three-dimensional actuations of kirigami patterns composed of magnetic-particles–polymer composites," *ACS Nano*, vol. 14, no. 12, no. 17589–17596, 2020.

[34] Y. Kim et al., "Telerobotic neurovascular interventions with magnetic manipulation," *Sci. Robot.*, vol. 7, no. 65, 2022, Art. no. eabg9907.

[35] Y. Kim, G. A. Parada, S. Liu, and X. Zhao, "Ferromagnetic soft continuum robots," *Sci. Robot.*, vol. 4, no. 33, 2019, Art. no. eaax7329.

[36] J. Wang, R. Wang, Z. K. Zhu Zhou, and D. Wang, "Untethered kirigami soft robots with programmable locomotion," *Appl. Phys. Rev.*, vol. 10, 2023, Art. no. 041405.

[37] J. Wang, D. Wang, L. Dong, M. Zhang, and G. Gu, "Analytical modeling and inverse design of centimeter-scale hard-magnetic soft robots," *IEEE Trans. Automat. Sci. Eng.*, early access, Sep. 2023, doi: 10.1109/TASE.2023.3313395.

[38] R. Zhao, Y. Kim, S. A. Chester, P. Sharma, and X. Zhao, "Mechanics of hard-magnetic soft materials," *J. Mechanics Phys. Solids*, vol. 124, pp. 244–263, 2019.

[39] X. Liang, H. Fu, and A. J. Crosby, "Phase-transforming metamaterial with magnetic interactions," *Proc. Nat. Acad. Sci. USA*, vol. 119, no. 1, 2022, Art. no. e2118161119.
[40] Y. Kim and X. Zhao, "Magnetic soft materials and robots," *Chem. Rev.*, vol. 122, no. 5, pp. 5317–5364, 2022.
[41] W. Li, T. Cheng, M. Ye, C. S. H. Ng, P. W. Y. Chiu, and Z. Li, "Kinematic modeling and visual servo control of a soft-bodied magnetic anchored and guided endoscope," *IEEE/ASME Trans. Mechatron.*, vol. 25, no. 3, pp. 1531–1542, Jun. 2020.
[42] D. Hua, X. Liu, S. Sun, M. A. Sotelo, Z. Li, and W. Li, "A magnetorheological fluid-filled soft crawling robot with magnetic actuation," *IEEE/ASME Trans. Mechatron.*, vol. 25, no. 6, pp. 2700–2710, Dec. 2020.
[43] W. Hu, G. Z. Lum, M. Mastrangeli, and M. Sitti, "Small-scale soft-bodied robot with multimodal locomotion," *Nature*, vol. 554, no. 7690, pp. 81–85, 2018.
[44] Y. Wang, X. Du, H. Zhang, Q. Zou, J. Law, and J. Yu, "Amphibious miniature soft jumping robot with on-demand in-flight maneuver," *Advanced Sci.*, vol. 10, 2023, Art. no. 2207493.
[45] L. S. Novelino, Q. Ze, S. Wu, G. H. Paulino, and R. Zhao, "Untethered control of functional origami microrobots with distributed actuation," *Proc. Nat. Acad. Sci. USA*, vol. 117, no. 39, pp. 24096–24101, 2020.
[46] Y. Yang, M. A. Dias, and D. P. Holmes, "Multistable kirigami for tunable architected materials," *Phys. Rev. Mater.*, vol. 2, no. 11, 2018, Art. no. 110601.
[47] Y. Tang, G. Lin, L. Han, S. Qiu, S. Yang, and J. Yin, "Design of hierarchically cut hinges for highly stretchable and reconfigurable metamaterials with enhanced strength," *Adv. Mater.*, vol. 27, no. 44, pp. 7181–7190, 2015.
[48] K. Seffen and S. Pellegrino, "Deployment dynamics of tape springs," *Proc. Roy. Soc. London Ser. A, Math. Phys. Eng. Sci.*, vol. 455, no. 1983, pp. 1003–1048, 1999.
[49] L. Yang, M. Zhang, Z. Yang, and L. Zhang, "Multimode control of a parallel-mobile-coil system for adaptable large-workspace microrobotic actuation," *IEEE/ASME Trans. Mechatron.*, vol. 28, no. 3, pp. 1662–1673, Jun. 2023.
[50] C. Wang, Y. Wu, X. Dong, M. Armacki, and M. Sitti, "In situ sensing physiological properties of biological tissues using wireless miniature soft robots," *Sci. Adv.*, vol. 9, no. 23, 2023, Art. no. eadg3988.

Ruichen Wang received the B.Eng. degree in mechanical engineering from the Chongqing University, Chongqing, China, in 2021. He is currently working toward the Ph.D. degree in mechanical engineering with the Shanghai Jiao Tong University, Shanghai, China.

His research interests include direct-ink-writing printing and soft robotics, especially the modeling and design of magnetic actuation robotics.

Jinqiang Wang received the B.Eng. degree in mechanical engineering from Hunan University, Changsha, China, in 2016, and the M.Eng. degree in mechanical engineering from Nanjing University, Nanjing, China, in 2019. He is currently working toward the Ph.D. degree in mechanical engineering with Shanghai Jiao Tong University, Shanghai, China.

His research interests include 4-D printing and soft robotics, especially the modeling and design of magnetic actuation robotics.

Zixiao Zhu received the B.Eng. degree in mechanical engineering in 2023 from Shanghai Jiao Tong University, Shanghai, China, where he is currently working toward the master's degree in mechanical engineering.

His research interests include multimaterial 3-D printing and path planning of magnetic actuation direct-ink-writing printing.

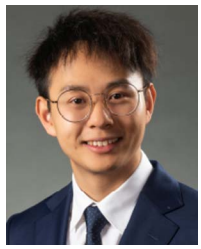

Dong Wang received the B.Eng. degree in mechanical engineering from Zhejiang University, China, in 2010, and the Ph.D. degree in mechanical engineering from Nanyang Technology University, Singapore, in 2015.

Since 2018, he has been with Shanghai Jiao Tong University, Shanghai, China, where he is currently an Associate Professor with the School of Mechanical Engineering. He is the author or coauthor of more than 50 publications. His research interests include soft robotics, 3-D and 4-D printing, and solid mechanics.